Do cataclastic deformation bands form parallel to lines of no finite elongation (LNFE) or zero extension directions?

Jonathan Imber[1]*, Tom Perry[1], Richard R. Jones[2] and Ruth H. Wightman[1,3]

[1]Department of Earth Sciences, Durham University, Durham, DH1 3LE, UK

[2]Geospatial Research Ltd., Department of Earth Sciences, Durham University, Durham, DH1 3LE, UK

[3]Now at: Midland Valley Exploration Ltd., 144 West George Street, Glasgow, G2 2HG, UK

*Corresponding author. Tel.: +44 (0)191 334 4307; fax: +44 (0)191 334 2301.

E-mail address: jonathan.imber@durham.ac.uk (J. Imber)

Abstract

Conjugate cataclastic deformation bands cut unconsolidated sand and gravel at McKinleyville, California, and dip shallowly towards the north-northeast and south-southwest. The acute dihedral angle between the two sets of deformation bands is 47° and is bisected by the sub-horizontal, north-northeast directed incremental and finite shortening directions. Trishear models of fault propagation folding above the McKinleyville fault predict two sets of LNFE (lines of no finite elongation) that plunge steeply and shallowly to the south and north. These predictions are inconsistent with deformation band orientations and suggest that deformation bands did not form parallel to these LNFE. During plane strain, zero extension directions with acute dihedral angles of 47° develop when the dilatancy rate ($dV/d\varepsilon_1$) is -4.3. Experimental dilatancy rates for Vosges sandstone (cohesion > 0)

and unconsolidated Hostun sand suggest the deformation bands either developed parallel to zero extension directions or in accordance with the Mohr-Coulomb criterion, assuming initial porosities of 22% and 39%, respectively. An empirical relationship between $dV/d\varepsilon_1$, relative density and mean stress suggests that dilatancy rates for Vosges sandstone overestimate $dV/d\varepsilon_1$ at McKinleyville. Deformation bands at McKinleyville likely developed either in a Mohr-Coulomb orientation, or an intermediate orientation bounded by the Mohr-Coulomb (θ_C) and Roscoe (θ_R) angles.

Keywords: strain, dilation, deformation band, high porosity sandstone

1. Introduction

Structural geologists typically invoke the Mohr-Coulomb failure criterion to explain the orientations of shear fractures (faults) based on assumptions (or measurements) of the angle of internal friction and the orientations of the principal stresses. The Mohr-Coulomb relationship predicts that the angle, θ_C, between the fault and the direction of the maximum principal stress, σ_1, is given by

$$\theta_C = \pi/4 - \varphi/2 \quad \text{(equation 1; e.g. see Bardet, 1990)}$$

where φ is the internal friction angle of the material. θ_C ("Mohr-Coulomb" orientation; Wolf et al., 2003) provides an accurate first-order description of the orientations of faults in different tectonic regimes (e.g. Anderson, 1951; Bésuelle and Rudnicki, 2004).

Despite the widespread acceptance of the Mohr-Coulomb failure criterion, attempts have been made to interpret fracture orientations in terms of strain geometry. Becker (1893) proposed that shear failure occurs parallel to planes of zero longitudinal strain, which were believed to coincide with circular sections of the finite strain ellipsoid. He hypothesised that: (1) rupture takes places along surfaces of maximum shear strain, and (2) that planes of maximum shear strain coincide with circular sections of the finite strain ellipsoid (Becker, 1893). This "strain ellipsoid" theory of rupture was eventually

47 discarded (Brace, 1961) due to the its inability to explain the orientations of shear failure surfaces
48 commonly observed in laboratory deformation experiments, and because in a general triaxial strain
49 ellipsoid (i.e. all three principal axes of finite strain have changed length) the surfaces of zero
50 longitudinal strain define elliptical cones (e.g. see Sarkarinejad et al., 2011, fig. 1), not circular
51 sections (Griggs, 1935).

52 Nevertheless, there has been renewed interest in using strain geometry to interpret shear fractures (e.g.
53 Allmendinger, 1998; Watterson 1999; Cardozo et al., 2005; Jin and Groshong, 2006). This motivation
54 stems in part from the advent of trishear models (Erslev 1991), which provide a detailed description of
55 the heterogeneous strain at propagating fault tips, and a desire to use this information to predict the
56 distribution and orientation of small-scale faults. A further motivation has been to develop a unified,
57 strain-based model for interpreting geological shear structures, which encompasses both brittle faults
58 (normally analysed in terms of stress) and macroscopically ductile shear zones (normally described in
59 terms of strain) (Watterson 1999). Two hypotheses have been suggested: (1) that the lines of no finite
60 elongation (LNFE) predicted by trishear models are proxies for minor shear fractures that develop at
61 the tips of propagating faults during forced folding (here referred to as the "LNFE hypothesis")
62 (Allmendinger, 1998); and (2) that shear fractures in rock, soil or other granular materials form
63 parallel to zero extension directions (here referred to as the "zero extension hypothesis") (Roscoe,
64 1970; Watterson, 1999).

65 LNFE are the lines within the finite strain ellipsoid whose deformed length is equal to their
66 undeformed length (Fig.1a) (Ramsay and Huber, 1983, p. 5). For a given finite strain, material lines
67 that currently lie parallel to a LNFE will have a strain history involving elongation and contraction
68 which have compensated each other; i.e. they are unlikely to have remained parallel to a LNFE
69 throughout their deformation history (Ramsay and Huber, 1983), particularly when the finite strain is
70 high. Zero extension directions are the directions in which the *rate* (or increment) of elongation is
71 zero and in plane strain loading their orientation is expressed by

72 $$\theta_R = \pi/4 - \psi/2 \quad \text{(equation 2; e.g. see Bardet, 1990)}$$

where θ_R ("Roscoe" orientation; Wolf et al., 2003) is the inclination of the zero extension directions with respect to the axis of maximum principal strain rate (or increment). ψ is the angle of dilation. For plane strain, $\sin\psi = -(d\varepsilon_1 + d\varepsilon_3) / (d\varepsilon_1 - d\varepsilon_3)$. $d\varepsilon_1$ and $d\varepsilon_3$ are the maximum and minimum principal strain rates (or increments), respectively (Fig. 1b) (Bardet, 1990).

The aim of this paper is to compare predictions of the LNFE and zero extension hypotheses with the orientations of two sets of apparently conjugate, cataclastic deformation bands that cut unconsolidated, late Pleistocene marine terrace sands at McKinleyville, northern California (Cashman and Cashman, 2000). There are three reasons why the structures at McKinleyville are suitable for this purpose. First, there is nothing unusual about the orientations of the deformation bands at McKinleyville, which have been described as indicative of "Coulomb fracture failure" (Carver and Aalto, 1992). If the LNFE and/or zero extension hypotheses are valid, they should be capable of explaining the orientation of these deformation bands. Second, the neotectonic loading configuration that led to the development of the cataclastic deformation bands is known, at least to a first order, and lends itself to trishear forward modelling. Finally, the shallow burial depth and unconsolidated nature of the host sediments at McKinleyville allow comparison of our findings with experimental and theoretical studies in soil mechanics, from which many of the observations and theories concerning the deformation of sand originated (e.g. Roscoe, 1970; Vermeer, 1990; Bardet 1990).

We start by summarising recent studies that suggest strain geometry can be used to predict shear fracture orientations, and then describe the cataclastic deformation bands at McKinleyville. Next, we compare the observed deformation band orientations with the predictions of the LNFE and zero extension hypotheses, before discussing our results in the light of experimental and theoretical findings in the soil mechanics literature. We conclude that cataclastic deformation bands at McKinleyville are unlikely to have developed parallel to LNFE or zero extension directions, but could plausibly have formed in a Mohr-Coulomb orientation, or at an angle intermediate between θ_C and θ_R.

2. Summary of previous work and basis for using strain geometry to predict shear fracture orientations

2.1. LNFE and shear fracture orientations

Allmendinger (1998) provided an intuitive explanation for why shear fractures might form along LNFE. This explanation is based on the observation that shear planes are directions of no finite elongation during simple shear, as exemplified by the card deck shearing experiment known to all structural geology students (Ramsay and Huber, 1983, fig. 1.1). Ramsay and Huber (1983, equation D.10) showed that the orientations of LNFE with respect to the principal axis of finite strain can be calculated if the quadratic extensions are known, using

$$\tan^2\alpha = \lambda_2(\lambda_1 - 1) / \lambda_1(1 - \lambda_2) \quad \text{(equation 3)}$$

where α is the angle between the LNFE and the maximum principal axis of finite strain (X), and λ_1 and λ_2 are the maximum and minimum quadratic extensions, respectively (Fig. 1a, inset). This equation can also be used to determine how the acute angle between the two sets of LNFE (2α) changes with the magnitude of finite strain (expressed by the ellipticity, R; see Ramsay and Huber, 1983, p. 31) (Fig. 1a).

Allmendinger (1998) and Jin and Groshong (2006) presented experimental observations to support the LNFE hypothesis. These authors found that the LNFE predicted by trishear models of forced folding above an extensional fault matched the orientations of minor fractures in scaled clay models (e.g. Withjack et al., 1990). In both cases, traces of steeply dipping shear fractures within the clay models were parallel to one set of (steeply plunging) LNFE (Allmendinger, 1998, fig. 9; Jin and Groshong, 2005, fig. 10). The second set of LNFE did not correspond to fractures in the clay models, but rotated passively during the deformation (Allmendinger 1998). Field observations also appear to be consistent with the LNFE hypothesis. Cardozo et al. (2005) compared LNFE orientations predicted by a trishear model with the orientations of minor faults on the limbs of the Rip Van Winkle anticline, a fault propagation fold in the Hudson Valley fold-and-thrust belt, eastern New York. Minor faults observed

123 in the forelimb of the anticline and the set of LNFE antithetic to the main fault plane were both
124 oriented parallel to steeply-dipping bedding planes. The authors concluded from the best-fit trishear
125 model that minor faults on the forelimb formed during a late stage of folding, at a point in the
126 deformation history when the antithetic set of LNFE were oriented parallel to bedding. However,
127 neither set of LNFE were consistent with the orientations of minor faults located in the footwall
128 syncline ahead of the propagating thrust (Cardozo et al., 2005, fig. 13b).

129 These observations lend support to the hypothesis that trishear-predicted LNFE are proxies for minor
130 shear planes, but raise two issues. First, the authors did not present a strain-based criterion to predict
131 whether shear fractures will develop parallel to one, or both, sets of LNFE. Second, although
132 comparisons between trishear models and minor shear fractures in clay models suggest that fracturing
133 occurs within regions of highest finite strain (Allmendinger, 1998; Jin and Groshong, 2006), there are
134 no criteria to predict at what magnitude of finite strain (i.e. at what stage during the development of a
135 fault propagation fold) minor shear fractures will initiate.

136

137 ## *2.2. Zero extension directions and shear fracture orientations*

138 The prediction that shear fractures form parallel to zero extension directions is based on two
139 requirements: (1) to maintain strain compatibility between a localised shear zone and its less-
140 deformed matrix; and (2) that the localised deformation within a shear zone must have its components
141 of principal strain rate (or strain increment) in the same ratio to each other as those of the bulk
142 deformation. If these conditions are met, assuming plastic flow occurs at a constant stress (the yield
143 stress) and the principal axes of stress and plastic strain rate (or strain increment) coincide, then
144 localised shear zones will develop parallel to planes in which the extension rate is zero (Bowden and
145 Jukes, 1972). Roscoe (1970) described a series of deformation experiments in which Leighton
146 Buzzard sand was deformed under a variety of plane strain loading configurations. These experiments,
147 in which the principal axes of stress and strain rate did not rotate, showed that “rupture surfaces”
148 (shear bands) within the sand formed parallel to one set of zero extension directions. In turn, the

orientations of the zero extension directions with respect to the axis of maximum principal strain rate depended upon the angle of dilation (e.g. Roscoe, 1970, figs 6, 7, 23 and 24) (equation 2).

Watterson (1999) used a Mohr circle construction to predict the orientations of zero extension directions during uniaxial and plane strain loading (e.g. Fig. 1b). Shear fractures that develop during uniaxial shortening experiments are typically inclined at ca. 30° to the shortening direction. The volume strain increment (dV) required for the zero extension directions to be inclined at 30° to the shortening direction is five times the maximum principal strain increment ($d\varepsilon_1$), i.e. $dV/d\varepsilon_1 = -5$ at the onset of fracture localisation (adopting the soil mechanics convention of shortening or contraction being positive and $dV/d\varepsilon_1$ being the "dilatancy rate"; Bolton, 1986). Application of the same dilatancy rate ($dV/d\varepsilon_1 = -5$) to plane strain loading results in zero extension directions that are inclined at 22° to the shortening direction, which would correspond to a normal fault dip of 68° (Watterson, 1999, fig. 6). These observations and arguments are consistent with the hypothesis that shear fractures develop parallel to zero extension directions. However, the dilatancy rates predicted above have not been verified experimentally (Watterson, 1999), nor is it clear the extent to which the requirements and assumptions described by Bowden and Jukes (1972) are met during natural deformation.

3. Cataclastic deformation bands at McKinleyville

3.1. Geological setting

The studied outcrop is situated near McKinleyville, Humboldt County, California and lies within the overriding North American plate at the southern end of the Cascadia Subduction Zone (CSZ). Here, the CSZ is associated with a Quaternary fold-and-thrust-belt that is 85-100 km wide and extends along the western edge of the North American accretionary margin. The fold-and-thrust belt is exposed onshore in northern California where it comprises the north-west trending Mad River and Little Salmon fault zones separated by the 30 km wide Freshwater syncline (Fig. 2a). Quaternary sedimentation took place within isolated depocentres associated with the rapidly growing folds and thrusts (Carver, 1992). Focal mechanisms in the Humboldt Bay region are primarily reverse faults

175 with some events having components of oblique- or strike-slip motion (McPherson, 1992). These
176 mechanisms are consistent with a horizontal, north to north-northeast directed incremental shortening
177 direction ($d\varepsilon_1$) and north to north-northeast directed S_{Hmax} (Kreemer et al., 2003; Heidbach et al., 2008)
178 (Fig. 2b).

179 The Mad River fault zone consists of multiple north-east dipping faults (including the McKinleyville
180 fault), which thrust Cretaceous basement rocks (Franciscan complex) over early Pleistocene
181 sediments (Falor Formation) (Fig. 2c; Carver, 1992). The principal faults dip 35° ± 10° towards the
182 north-east and may merge at depth as a single strand (Carver, 1992; McCrory, 1996). Carver (1987)
183 attributes the development of asymmetric, NW-SE trending anticlines associated with the Mad River
184 fault zone to fault propagation folding. The McKinleyville fault has experienced an average slip rate
185 of 0.6 ± 0.2 mm/yr over the last ca. 200 ka (Petersen et al., 1996), whilst Clarke and Carver (1992)
186 have reported at least two Holocene slip events, each of which resulted in ca. 3.5 m of dip slip along
187 the McKinleyville fault.

188 Near the coast, the McKinleyville fault comprises two distinct segments (Fig. 3a) that cut a sequence
189 (known informally as the "Mouth of Mad unit"; Harvey and Weppner, 1992) of unconsolidated
190 nearshore and strand-plain sands that are locally inter-bedded with gravel beds and lenses and are
191 overlain by < 5 m of mud-rich bay deposits (Miller and Morrison, 1988; Harvey and Weppner, 1992).
192 These sediments were deposited during growth of the Quaternary fold-and-thrust belt, and are
193 bounded above and below by unconformities (Harvey and Weppner, 1992). The Mouth of Mad unit is
194 ca. 30 m thick and has been dated at 176 ± 33 ka by a single thermoluminescence date obtained from
195 the mud-rich bay deposits (Berger et al., 1991).

196 We focus on NNE-SSW trending sea cliff exposures (located at 40º58'17''N; 124º07'07''W), where
197 reverse faulting on the southern segment of the McKinleyville fault has created a ca. 150 m-wide belt
198 of cataclastic deformation bands within the Mouth of Mad unit (Fig. 3b). Bedding is sub-horizontal
199 (albeit locally cross-bedded) in the southern part of the cliff section, increasing in dip to ca. 20° SW,
200 adjacent to the southern segment of the McKinleyville fault (Miller and Morrison, 1988; Carver and

201 Aalto, 1992). There is no evidence that the bedding has been overturned within the studied exposures.
202 The maximum burial depth was 50 m, limiting the confining pressure for the development of the
203 cataclastic deformation bands to ≤ 1 MPa (Cashman and Cashman, 2000). Unfortunately, the trace of
204 the southern segment of the McKinleyville fault has been obscured by a recent landslip, ca. 50 m wide
205 (Fig. 3b). Assuming that the fault plane dips at 35° (Petersen et al., 1996), and that the sea cliffs are
206 30 m high, this lack of exposure gives rise to a ca. 10 m horizontal uncertainty in the location of the
207 fault trace at the coast. However, this uncertainty does not affect our overall conclusion that the
208 deformation bands are unlikely to have developed parallel to LNFE or zero extension directions
209 (sections 4 and 5).

210

211 ### *3.2. Deformation band geometries*

212 The cataclastic deformation bands form two prominent sets that dip towards the north-east and south-
213 west, i.e. synthetic and antithetic to the McKinleyville Fault, respectively (Cashman and Cashman,
214 2000) (Fig. 4). A third, albeit less prominent set of sub-horizontal dilation bands is also present (Du
215 Bernard et al., 2002). In order to collect an unbiased set of orientation data from the ca. 30 m high
216 exposures, we carried out a terrestrial laser scan (ground-based LIDAR) survey of the sea cliffs (e.g.
217 Jones et al. 2009). The resulting point-cloud data were textured using high-resolution, georeferenced
218 digital photographs, allowing us to pick the traces of individual cataclastic deformation bands.
219 Dilation bands were not clearly imaged within the textured point cloud data, so were not picked. We
220 then used the relief on each deformation band trace to extrapolate a best-fit plane a short distance
221 into/out of the outcrop (Jones et al., 2008). We sampled the orientations of 2256 deformation band
222 planes, with a combined trace length of in excess of 3.7 km, along the ca. 150 m long NNE-SSW
223 oriented exposure. A qualitative cross-check was made between the LIDAR-derived deformation
224 band orientations and a subset of deformation band orientations measured directly in the field.

225 The two sets of cataclastic deformation bands mutually cross-cut each other, suggesting that both sets
226 developed during the same deformation event (Fig. 4a). Individual deformation bands are sub-planar

features and occur singly, or form braided clusters up to 10 cm thick. Clusters of deformation bands are locally observed to displace gravel lenses or earlier-formed deformation bands by up to a few tens of centimetres, consistently in a reverse sense (Cashman and Cashman, 2000) (Fig. 4b). Figure 4c is a lower hemisphere equal area stereoplot showing poles to cataclastic deformation bands from across the entire outcrop. There is some scatter within this bulk dataset, but there are two distinct clusters associated with the north-east and south-west dipping bands. Inspection of high resolution digital photographs suggests there is no systematic change in the orientations of deformation bands at the interface between sands and inter-bedded gravel beds and lenses within the Mouth of Mad unit (Fig. 4b). The mean orientations have been estimated from a contoured stereoplot produced using R.J. Holcombe's GEOrient software (Fig. 4d). A greater degree of accuracy is not required for the purposes of our analysis (sections 4 and 5). The two sets of deformation bands have mean dips of 21° towards 033° and 26° towards 200°, respectively. The acute dihedral angle between these two clusters is 47°, which is bisected by a line that plunges at 03° towards an azimuth of 206° (Fig. 4c, d). This acute bisector is sub-parallel to the regional incremental shortening direction ($d\varepsilon_1$) and S_{Hmax} (Kreemer et al., 2003; Heidbach et al., 2008) (Fig. 2b). From this relationship, and the local and regional thrust geometries in Figure 2a, c, we infer that incremental and finite shortening directions are both sub-horizontal and oriented approximately N-S to NNE-SSW. Thus, the sub-vertical, NNE-SSW trending cliff section is approximately parallel to: (1) the plane containing $d\varepsilon_1$ and $d\varepsilon_3$, the sub-horizontal and sub-vertical incremental shortening and extension directions, respectively; and (2) the plane containing Z and X, the sub-horizontal and sub-vertical finite shortening and extension directions, respectively. In reality, there is likely to be an angular difference between the incremental and finite strain axes due to the transpressional nature of the regional deformation (e.g. Fig. 2a); however, rotation of the finite strain axes is likely to be small given the low magnitude of bulk strain within the exposed outcrop at the time of deformation band formation (sections 3.3 and 4).

To assess the spatial variation in deformation band orientations across the outcrop, we sub-sampled the cataclastic deformation band orientations in 5 m intervals from north to south along the cliff section. The mean deformation band orientations, acute dihedral angle and bisector orientation within

each 5 m block were estimated from contoured stereoplots (see above) and are summarised in Fig. 5 and listed in Table 1. Gaps in the data relate to areas of no exposure associated with landslips (combined interval of 51 m), or intervals where two clusters of deformation bands cannot be defined on a stereoplot (combined interval of 25 m). Apart from the northernmost interval (15-20 m from start of section), which displays steep deformation band dips towards the northwest, there are no systematic changes in the mean orientations of the deformation band clusters, the value of the acute dihedral angle or the orientation of the acute bisector across the outcrop (Fig. 5).

3.3. Deformation band microstructure and finite strain

Cashman and Cashman (2000) have described the microstructure of the cataclastic deformation bands and compared this with the microstructure of undeformed sand from outside the bands. Undeformed sand has 22-23% porosity. The sand is poorly cemented by clay minerals, iron oxides and organic material (Du Bernard et al., 2002), but has little cohesion. Cements are preferentially concentrated along deformation bands. Du Bernard et al. (2002) summed measured clay content and residual porosity to obtain an upper bound on the porosity of undeformed sand of 38%, assuming any clay contained within the sand was infiltrated after deformation band formation. Within a deformation band that dips moderately to the north-east, has 39.5 cm of reverse-dip separation and ranges from 1.5 to 8 cm in width, skeleton porosity (pore space + authigenic phases) drops to 10%. According to Cashman and Cashman (2000), this volume reduction occurred due to compaction and closing of pore space within the cataclastic deformation bands during shearing. Cashman and Cashman (2000) carried out Fry analysis on samples adjacent to and within deformation bands. They found that strain ellipses outside the deformation bands are approximately equant (i.e. $R \sim 1$, implying negligible finite distortion), whilst strain ellipses within deformation bands have mean ellipticities (R) of 1.3 ± 0.2 (1 standard deviation), with minimum and maximum values of 1.1 and 1.7, respectively (Cashman and Cashman, 2000, fig. 6). The finite extension directions are oriented $27° \pm 5.6°$ (1 standard deviation) from the deformation band boundaries, and the sense of rotation of strain ellipses is consistent with

reverse slip on the deformation band shear zone (Cashman and Cashman, 2000, fig. 6). These observations suggest that strain had localized along the cataclastic deformation bands before detectable (at least using the Fry method) finite distortions had accumulated within the wall rocks. In other words, the magnitude of bulk strain within the Mouth of Mad unit is likely to have been low at the time of deformation band localization.

4. Did the cataclastic deformation bands at McKinleyville form along LNFE?

In this section, we test the hypothesis that lines of no finite elongation (LNFE) predicted by trishear models are proxies for minor shear fractures that develop at the tips of propagating faults during forced folding. In principle, trishear inverse modelling can be used to constrain a best-fit trishear model (e.g. Allmendinger, 1998; Cardozo et al., 2011). However, the cross-bedded and intermittently-exposed nature of the Mouth of Mad unit makes it difficult to trace individual beds, or groups of beds, for any distance across the studied outcrop. We therefore adopt a forward modelling approach using area-conserving, two-dimensional trishear to predict the orientations of LNFE near the tip of the McKinleyville fault, and compare these predictions with observed deformation band orientations. Given the limitations of forward modelling, we then use the relationship expressed in equation (3) to back-calculate the magnitude of bulk distortional strain (expressed as ellipticity, Rxz) required to produce the two sets of LNFE with an acute dihedral angle (2α) comparable to that of the deformation bands (Fig. 1a). If the hypothesis that both sets of deformation bands formed parallel to these LNFE is correct, the calculated bulk distortional strain (expressed as ellipticity) should be no greater than the ellipticities estimated by Fry analysis (Cashman and Cashman, 2000).

4.1. Comparison with two-dimensional trishear models

We used the trishear forward modelling functionality within Midland Valley Exploration's 2DMove software to predict the magnitude of bulk finite strain (expressed by the ellipticity, Rxz) and LNFE orientations within the Mouth of Mad unit. Figure 6 shows the geometry of the trishear models. The models are 35 m thick and are oriented north-northeast-south-southwest (approximate dip lines). The thrust plane dips at 35° (cf. Petersen et al., 1996). Age dating shows that the Mouth of Mad unit was deposited during growth of the regional fold-and-thrust belt (section 3.1). However, we did not observe unequivocal field evidence for growth (thickening) within the Mouth of Mad unit toward the footwall of the McKinleyville fault; for simplicity, all strata were therefore modelled as being pre-growth.

We conducted tests using a range of different apical angles (50°, 70° and 90°) and maximum thrust displacements (10 m, 20 m, 30 m, 40 m and 56 m). 56 m displacement is a reasonable upper limit on the post-late Pleistocene displacement along the southern segment of the McKinleyville fault, assuming that slip was partitioned between the northern and southern fault segments (section 3.1; Fig. 2). A larger apical angle results in a wider zone of trishear deformation, whilst a bigger thrust displacement gives rise to larger magnitudes of finite strain in the hanging wall and footwall. We selected a propagation-slip (p/s) ratio of 1.6, which is mid-way between the values used by Jin and Groshong (2006) to model deformation of massive sandstone (p/s = 1.2) and interbedded carbonate-clastic (p/s = 2.0) sequences. In general, higher p/s ratios lead to a greater degree of rigid-body translation and lower amounts of wall rock strain.

Figure 7 shows how the ellipticities (R) vary with distance along the section for trishear models with apical angles of 50° and 90°, and maximum thrust displacements of 10 m (Fig. 7a) and 56 m (Fig. 7b). We have estimated the location of the landslip (grey band) and extent of the studied outcrop (dashed line) (Fig. 7) by comparing the modelled bed dips with those observed at McKinleyville (section 3.1). Ellipticities have been plotted at ca. 5 m intervals along the topmost layer shown in Figure 6. For models with maximum thrust displacements of 10 m and 56 m, the maximum ellipticity predicted

329 within the exposed part of the outcrop is ca. 1.2 (Fig. 7). The ellipticities decrease to negligible values
330 southward across the studied section. This prediction is consistent with the observed decrease in bed
331 dips southward away from the southern segment of the McKinleyville fault (section 3.1), and provides
332 confidence that trishear is appropriate to model strains at the tip of the McKinleyville fault.

333 Figure 8 shows how the orientations of the two sets of LNFE, the dihedral angle between LNFE (2α)
334 and the plunge of the acute bisector (i.e. the line that bisects the acute dihedral angle between pairs of
335 LNFE) vary with distance along the section for trishear models with apical angles of 50° and 90°, and
336 maximum thrust displacements of 10 m and 56 m. Positive angles refer to southward plunging LNFE
337 and acute bisectors; negative angles refer to northward plunges. These modelled attributes can be
338 compared directly to the field observations (Fig. 5, Table 1). We have again estimated the location of
339 the landslip (grey band) and extent of the studied outcrop (dashed line) in each model (Fig. 8) by
340 comparing the predicted bed dips with those observed at McKinleyville (section 3.1). Data are plotted
341 at ca. 5 m intervals along the topmost layer shown in Figure 6 (cf. Table 1).

342 In models with a maximum thrust offset of 10 m (Fig. 8a, b), the inclination of the southward-
343 plunging set of LNFE increases from 30-40° at the northern end of the model to 70-80° in the south.
344 There is little correspondence between the plunges of these LNFE and the southward-dipping
345 deformation bands, although this conclusion is sensitive to the estimated location of the landslip in the
346 models (Fig. 8a, b). By contrast, the inclination of the northward-plunging set of LNFE decreases
347 from 60-70° in the north to 15-20° in the south (Fig. 8a, b). For models with a trishear apical angle of
348 90°, there is good correspondence between the northward-plunging set of LNFE and the northward-
349 dipping set of deformation bands at the southern end of the studied section (Figs 4, 8b, Table 1).

350 In models with a maximum thrust offset of 56 m (Fig. 8c, d), the southward-plunging set of LNFE is
351 characterised by plunges that range from 25-85° in the hanging wall of the thrust (i.e. at the northern
352 end of the studied section), and 80-90° in the footwall. These LNFE plunge more steeply than typical
353 southward-dipping deformation bands. The plunge of the northward-plunging set of LNFE ranges
354 from 75-45° in the hanging wall of the thrust, to 5-30° in the footwall. Most of the northward-

355 plunging LNFE are shallower than northward-dipping deformation bands exposed in the footwall
356 section (Figs 4, 8c, d, Table 1). However, this conclusion is again sensitive to the estimated location
357 of the landslip in the models (Fig. 8c, d).

358 The dihedral angle (2α) and the plunge of the acute bisector between pairs of LNFE should
359 correspond to the dihedral angle and acute bisector between the two sets of deformation bands (Fig. 5,
360 Table 1) if, at any point along the studied section, both sets of deformation bands formed parallel to
361 LNFE. In all models, the dihedral angle between LNFE (2α) increases from north to south, with
362 values ranging from ca. 25° adjacent to the thrust tip (e.g. Fig. 8c), to 80-90° in the southern part of
363 the studied section (Fig. 8). The plunge of the acute bisector between pairs of LNFE ranges from 45-
364 90°, which is significantly more than the sub-horizontal plunge of the acute bisector between the two
365 sets of deformation bands (Fig 5p). At no point in the models do the dihedral angle (2α) *and* plunge of
366 the acute bisector both correspond to typical values associated with the deformation bands (ca. 47°
367 and 05°, respectively; Fig. 4, Table 1). These results suggest either that the trishear parameters used in
368 this study are not appropriate, or that the two sets of deformation bands do not develop parallel to
369 LNFE.

370

371 ## *4.2. Analysis of deformation band dihedral angles*

372 To test these conclusions, we assume *a priori* that the cataclastic deformation bands developed
373 parallel to LNFE. We use the acute dihedral angles measured between sets of deformation bands
374 within each 5 m interval (Fig. 5, Table 1) to calculate the magnitude of bulk distortional strain
375 (expressed by ellipticity, Rxz) required to produce two sets of LNFE with this dihedral angle
376 (equation 3 and Fig. 1a). The calculated ellipticities are then compared with the ellipticities measured
377 using the Fry method by Cashman and Cashman (2000). This analysis makes no assumptions about
378 the loading configuration at the time of deformation band localisation and is independent of the
379 trishear model set-up.

Figure 9 shows that for a constant area deformation, the relationship expressed in equation 3 consistently predicts ellipticities that are between 2 and 12 times greater than the ellipticities measured within cataclastic deformation bands by Cashman and Cashman (2000) (1.3 ± 0.2; Fig. 9). In other words, the magnitude of *bulk* distortion required for the deformation bands (in their present-day orientations) to have developed parallel to LNFE would need to be greater than the *local* distortion measured *within* deformation bands. Bulk distortions resulting in large ellipticities ($2 < R < 14$; Fig. 9) prior to and during localisation of deformation bands should be evident from Fry analysis of wall rock samples; however, negligible strains have been recorded within the wall rocks ($R \sim 1$; section 3.3) (Cashman and Cashman, 2000). It is difficult to envisage a scenario in which the bulk strains recorded by the wall rock ellipticities are greater than the strains recorded within deformation bands, along which slip has localised. It could be argued that the deformation bands formed along LNFE at lower bulk strains (i.e. with a larger dihedral angle) and that subsequent bulk distortional strain reduced the dihedral angle between the two sets of deformation bands. However, this suggestion is again inconsistent with the low ellipticities recorded in the wall rocks. The simplest conclusion – that does not require special circumstances for which there is little compelling evidence – is that the cataclastic deformation bands at McKinleyville did *not* form parallel to lines of no finite elongation.

5. Did the cataclastic deformation bands at McKinleyville form along zero extension directions?

So far, we have neglected the effects of volume strain (dilatancy) during deformation band localisation. Dilatancy influences the orientations of zero extension directions (equation 2) and is an important process during deformation band formation (Roscoe, 1970; Aydin et al., 2006). We now apply the Mohr construction presented by Bowden and Jukes (1972), Bolton (1986) and adapted by Watterson (1999) to investigate the effects of dilatancy on the orientations of zero extension directions in the Mouth of Mad unit. We estimate the dilatancy rate ($dV/d\varepsilon_1$) required to produce the

406 observed deformation band orientations by assuming *a priori* that the two sets of cataclastic
407 deformation bands formed parallel to zero extension directions (i.e. $\theta_R = 23.5°$, equation 2). $dV/d\varepsilon_1$ so
408 determined can be compared with dilatancy rates obtained from experimental studies.

409

410 ## *5.1. Analysis of volume strain*

411 We adopt the soil mechanics convention that contraction and shortening are positive and assume that:
412 (1) the maximum principal strain increment, $d\varepsilon_1$, is sub-horizontal and parallel to the shortening
413 direction; and (2) the minimum principal strain increment, $d\varepsilon_3$, is extensional and sub-vertical (section
414 3.2). Incremental volume strains (dV) are expressed by $dV = d\varepsilon_1 + d\varepsilon_2 + d\varepsilon_3$. We follow Watterson
415 (1999) in assuming that the dilational component of extension is parallel to $d\varepsilon_3$ during plane strain,
416 and there is no dilational component along $d\varepsilon_1$ or $d\varepsilon_2$.

417 If both sets of deformation bands developed along zero extension directions, the angle between $d\varepsilon_1$
418 and either of the zero extension directions measured in the $d\varepsilon_1 d\varepsilon_3$ plane (θ_R) is given by half the
419 measured acute dihedral angle (Fig. 1b). Double angles are used in the Mohr construction, so the zero
420 extension directions in the $d\varepsilon_1 d\varepsilon_3$ plane can be found at the point where a line drawn from the centre
421 of the Mohr's circle, at an angle $2\theta_R$ measured anticlockwise from $d\varepsilon_1$ intersects the vertical axis at $d\varepsilon$
422 = 0 (Fig. 1c). An incremental volume increase will shift the centre of the Mohr's circle to the left;
423 volume strains that produce zero extension directions consistent with the observed deformation band
424 geometries can therefore be deduced from the Mohr diagram (Fig. 1b).

425 Figure 10a shows that isovolumetric plane strain deformation results in two sets of zero extension
426 directions at 45° to $d\varepsilon_1$ (i.e., $2\theta_R = 90°$) (Watterson, 1999). It can be seen from the geometry of the
427 Mohr diagram that an incremental volume *increase* is required to produce an acute dihedral angle
428 between the two sets of zero extension directions (Fig. 10a). Assuming plane strain loading, the
429 incremental volume strain (dV) as a proportion of $d\varepsilon_1$ required to produce an acute angle ($2\theta_R$) of 47°
430 (equivalent to the mean dihedral angle between the two sets of deformation bands; Fig. 4) between the
431 zero extension directions is $dV/d\varepsilon_1 = -4.3$ (Fig. 10a). This value equates to a dilation angle (ψ) of 43°,

and is similar to $dV/d\varepsilon_1 = -5$, which was calculated by Watterson (1999) to explain the orientations of shear fractures that develop in uniaxial shortening experiments (section 2.2). For oblate strain (which, it could be argued, is more applicable than plane strain to transpressive deformation; Fig. 2a), a dilatancy rate of -9.6 would be required to produce an angle of 47° between zero extension directions. By way of comparison, a friction angle (φ) of 43° would be required for the two sets of deformation bands to have developed in a "Mohr-Coulomb" orientation (equation 1). Figure 10b shows the predicted spatial variation in dilatancy rate, based on variation in dihedral angle between the two sets of cataclastic deformation bands from north to south along the section (Fig. 5, Table 1). $dV/d\varepsilon_1$ ranges from -12 approximately two-thirds of the way along the section to -1.1 at the northernmost point. The mean value is -4.7.

5.2. Comparison with experimental studies of deformation band localisation in poorly consolidated sandstone and unconsolidated sand

There is geological evidence for dilatancy during deformation band localisation at McKinleyville. Du Bernard et al. (2002) argued that the lack of macroscopic shear offset along sub-horizontal bands (section 3.2) is consistent with a predominantly opening-mode failure. This finding is supported by microstructural observations, which show that the porosity within these dilation bands is 7% higher than that of the host sand. Field relationships suggest that dilation bands developed in the tensile quadrants of adjacent cataclastic deformation bands (Du Bernard et al., 2002, figs 2 and 6). However, our limited observations of localised dilation bands provide little information on the *bulk* volume strains that controlled the orientations of zero extension directions at the onset of deformation band localisation. We therefore consider previous laboratory deformation experiments that allow direct estimates of the incremental volume strain (dV) and axial shortening ($d\varepsilon_1$) during and prior to deformation band localisation.

Bésuelle et al. (2000) performed a series of triaxial deformation experiments on specimens of Vosges sandstone at confining pressures of 0.1 and 10 MPa, and then at further increments of 10 MPa up to a

458 maximum confining pressure of 60 MPa. The first two experiments encompass the likely range of
459 confining pressures (≤ 1 MPa) experienced by the Mouth of Mad unit. The Vosges sandstone is
460 poorly cemented but, unlike the Mouth of Mad unit, has some cohesion due to suturing of grains. It
461 has a porosity of ca. 22% (Bésuelle et al., 2000), which is similar to the lower bound on the porosity
462 of undeformed sands at McKinleyville (22-23%).

463 Desrues and Viggiani (2004) described the results of biaxial deformation experiments on
464 unconsolidated Hostun sand at confining pressures between 0.1 and 0.8 MPa. The initial porosity was
465 ca. 39%, which is close to the upper bound on the porosity of undeformed sands at McKinleyville
466 (38%) (section 3.3). For both sets of experiments, we have used published graphs of: (1) deviatoric
467 stress ($\sigma 1 - \sigma_3$) or stress ratio ($[\sigma_1 - \sigma_3] / [\sigma_1 + \sigma_3]$) versus axial strain; and (2) volume strain versus
468 axial strain to estimate the dilatancy rate ($dV/d\varepsilon_1$) during the final increment of axial shortening prior
469 to peak stress (see Bésuelle et al., 2000, fig. 3; Desrues and Viggiani, 2004, figs 11 and 13). In each
470 case, this increment corresponds to 10% of the total axial shortening at peak stress. For plane strain
471 (biaxial) experiments, we also estimated the angle of dilation (ψ) according to

472 $$\sin\psi = - (dV/d\varepsilon_1) / (2 - dV/d\varepsilon_1)$$ (equation 4; Schanz and Vermeer, 1996).

473 Measured in this way, we obtain estimates of $dV/d\varepsilon_1$ (and ψ) immediately prior to peak stress. For
474 Vosges sandstone, deformation band localisation takes place at a decreasing fraction of peak stress as
475 the confining pressure increases (see Bésuelle et al., 2000, fig. 11), but this effect does not greatly
476 influence our estimates of $dV/d\varepsilon_1$ at low the confining pressures relevant to McKinleyville.

477 For Vosges sandstone with an initial porosity of 22%, $dV/d\varepsilon_1$ is ca. -8.5 and -2.8 at confining
478 pressures of 0.1 and 10 MPa, respectively. These dilatancy rates bracket $dV/d\varepsilon_1 = -4.3$ predicted for
479 plane strain deformation within the Mouth of Mad unit at ca. 1 MPa confining pressure. At higher
480 confining pressures of 20, 30 and 40 MPa, dilatancy rates are -1.5, -0.8 and -0.08, respectively (Fig.
481 11a). The dilatancy rate at 50 MPa confining pressure is close to zero, whilst at 60 MPa, the sandstone
482 shows continual contraction. For triaxial loading, these dilatancy rates would give rise to zero
483 extension directions inclined at between 25° and 54° to the shortening axis at confining pressures

484 between 0.1 and 40 MPa (Fig. 11b). By contrast, the Mohr-Coulomb relationship (Bésuelle et al.,
485 2000, fig. 20) predicts that the deformation bands should be oriented at between 24° and 54° with
486 respect to the maximum principal stress at confining pressures between 0.1 and 60 MPa. Overall, the
487 majority of deformation band orientations appear to lie between the limits defined by the Roscoe and
488 Mohr-Coulomb orientations, consistent with theoretical predictions (Fig. 11b and section 6).

489 Hostun sand, with an initial porosity of 39%, is characterised by dilatancy rates ($dV/d\varepsilon_1$) of -0.60, -
490 0.55, -0.46 and -0.34 at confining pressures of 0.1, 0.2, 0.4 and 0.8 MPa, respectively. These values
491 correspond to dilation angles of 13°,13°, 11° and 8.4° (Fig. 11a); all are significantly lower than the
492 dilation angle (ψ = 43°) required by the zero extension hypothesis to explain deformation band
493 orientations at McKinleyville (section 5.1). For biaxial loading, these dilatancy rates would give rise
494 to zero extension directions ("Roscoe" orientations) inclined at between 38° and 41° to the shortening
495 axis at confining pressures between 0.1 and 0.8 MPa (Fig. 11c). By contrast, the Mohr-Coulomb
496 relationship (Desrues & Viggiani, 2004, their table IV) predicts that the deformation bands should be
497 oriented at between 21° and 24° with respect to the maximum principal stress at confining pressures
498 between 0.1 and 0.8 MPa. Overall, the observed deformation band orientations appear to lie between
499 the limits defined by the Roscoe and Mohr-Coulomb orientations, and are closest to the Mohr-
500 Coulomb orientation at low confining pressures (Fig. 11c).

501 The two sets of experiments highlight the well-known result that dilatancy rate is sensitive to both
502 confining pressure (Watterson, 1999) and initial porosity (e.g. Bolton, 1986). The experiments
503 described by Bésuelle et al. (2000) suggest that high dilatancy rates (in the order of $dV/d\varepsilon_1$ = -4.3, as
504 calculated in section 5.1) may have been possible during deformation at low confining pressure within
505 the Mouth of Mad unit *provided* the initial porosity was close to the estimated lower bound of 22-23%
506 (Fig. 11a). On the other hand, biaxial deformation of Hostun sand suggests that the deformation bands
507 at McKinleyville could have developed in a Mohr-Coulomb orientation (i.e. θ_C = 23.5°, equation 1),
508 assuming an initial porosity of 39% (close to the upper bound), peak friction angle (φ) of 43° and
509 confining pressure of 0.8 MPa (Fig. 11c). It is therefore important to consider the differences in
510 mechanical behaviour between Vosges sandstone (cohesion > 0) and unconsolidated sand (Wang and

511 Leung, 2008). A well-established empirical relationship between dilatancy rate, mean stress and
512 relative density can be applied to Desrues and Viggiani's (2004) results for Hostun sand to estimate
513 the dilatancy rate of unconsolidated sand with an initial porosity of 22% (Bolton, 1986, his equation
514 17, using minimum and maximum void ratios for Hostun sand obtained from Flavigny et al., 1990 and
515 mean stresses obtained from Desrues et al., 2007, their Tables 1 and 2). This relationship indicates a
516 threefold (or smaller) increase in dilatancy rate relative to Hostun sand with an initial porosity of 39%,
517 equating to $dV/d\varepsilon_1$ of ca. -1.5 and -1 at a confining pressures of 0.1 and 0.8 MPa, respectively.
518 Although imprecise, this result suggests that experimental data for Vosges sandstone overestimates
519 the likely range of dilatancy rates that existed within the Mouth of Mad unit. Indeed, the dilatancy rate
520 obtained for Vosges sandstone appears to be significantly higher than dilatancy rates obtained from
521 other porous sandstones (Nguyen et al., 2011). Finally, both sets of experiments show that
522 deformation band orientations are not perfectly consistent with *either* the Roscoe *or* Mohr-Coulomb
523 orientations across the entire range of confining pressures tested. We conclude that the experimental
524 data lend, at best, equivocal support to the hypothesis that the cataclastic deformation bands at
525 McKinleyville developed along zero extension directions. We therefore turn to theoretical studies of
526 displacement discontinuities and strain localisation in granular materials to further evaluate the
527 relationship between deformation band orientations and zero extension directions.

528

529 ## 6. Discussion

530 Houlsby and Wroth (1980) investigated the restrictions placed on the orientation of an infinitesimally
531 thick deformation band by the constitutive behaviours of different materials undergoing plane strain
532 deformation. They assumed that the longitudinal strain rate (or strain increment) within the
533 deformation band is infinitesimally small and that the principal axes of stress and strain rate coincide.
534 Static equilibrium across the boundaries of the deformation band requires that the tractions on the
535 plane of the deformation band should be the same within the band and surrounding regions. For
536 granular materials with an associated flow rule, the friction angle and angle of dilation are the same,

537 i.e. $\varphi = \psi$ (e.g. Vermeer and de Borst, 1984, p. 8). In this case, Houlsby and Wroth (1980)
538 demonstrated that deformation bands can only develop along zero extension directions. By contrast,
539 deformation bands in granular materials with a non-associated flow rule ($\psi < \varphi$) can either develop
540 parallel to the zero extension directions, or oblique to these directions such that the deformation band
541 undergoes longitudinal shortening or extension (Houlsby and Wroth, 1980). Unconsolidated sands
542 such as the Mouth of Mad unit possess negligible cohesion and are most likely characterised by non-
543 associated flow in which $\psi < \varphi$ (Vermeer and de Borst, 1984, p. 28). The possibility that deformation
544 bands formed oblique to the zero extension directions is therefore to be expected at McKinleyville.

545 Vermeer (1990 and references therein) reviewed experimental data on deformation band localisation
546 in granular materials during plane strain (biaxial) loading. He showed that experimental attempts to
547 prove deformation bands develop in either Mohr-Coulomb or Roscoe orientations were inconclusive.
548 The data showed that deformation bands in homogeneous granular materials undergoing biaxial
549 deformation with fixed principal stress directions are oriented at a specific angle, which varies
550 according to grain size, between the limits θ_C (equation 1) and θ_R, (equation 2). In general,
551 deformation band orientations change from θ_C to θ_R with increasing grain size (Arthur et al., 1977;
552 Vermeer, 1990; Wolf et al., 2003), i.e. deformation bands might be expected to form parallel to zero
553 extension directions in coarse granular materials, such as gravel beds or lenses.

554 Vermeer (1990) used a bifurcation analysis including the effects of elastic unloading within material
555 outside the deformation band to demonstrate that all orientations of deformation bands between θ_C to
556 θ_R are admissible. Extending this analysis to the post-failure regime shows that localisation of
557 deformation bands with a Mohr-Coulomb orientation (θ_C) results in softening, and a discontinuity in
558 deformation band-parallel stresses inside and outside the band. By contrast, localisation of
559 deformation bands with a Roscoe orientation (θ_R) neither results in softening, nor a stress
560 discontinuity (Vermeer, 1990, figs 7 and 8). Deformation band width is related to particle size, so a
561 drop in band-parallel stress would yield large out-of-balance forces at the terminations of Mohr-
562 Coulomb-type deformation bands in coarse grained aggregates. Such forces would be minimised at
563 the tips of Roscoe-type deformation bands. Vermeer (1990) proposed that bands with Roscoe

564 orientations are likely to develop in coarse grained specimens undergoing biaxial deformation, an
565 argument that applies to laboratory experiments in which the deformation bands interact with cell
566 boundaries, and particle sizes are comparable to the thickness of the rubber membrane surrounding
567 the samples (Vermeer, 1990). At McKinleyville, grain size does not appear to be an important
568 influence on deformation band orientation (section 3.2) and the thickness of deformation bands is
569 negligible compared to the dimensions of the Mouth of Mad unit. Furthermore, the proximity to the
570 free surface at the time of deformation band formation suggests out-of-balance forces may not have
571 been a critical control on the orientations of long, continuous deformation bands. We therefore see no
572 compelling argument that the deformation bands at McKinleyville necessarily developed parallel to
573 zero extension directions, even within coarse gravel lenses. A more likely scenario based on the
574 experimental results and this brief review of theoretical studies, is that the deformation bands at
575 McKinleyville formed either in a Mohr-Coulomb orientation, or at an intermediate angle between θ_C
576 and θ_R.

577 An immediate implication of our findings is that using kinematic or strain-based models to predict the
578 orientations of minor shear fracture orientations using either LNFE or zero extension directions
579 should be treated with caution. However, Roscoe angles obtained from zero extension directions may
580 provide one limit on potential deformation band orientations, the other limit being given by the Mohr-
581 Coulomb relationship. Our attempt to apply the results of deformation experiments to McKinleyville
582 highlights the importance of constitutive behaviour (expressed here by φ and ψ, which are broadly
583 analogous to the friction coefficient, μ, and dilatancy factor, β, used in bifurcation analyses, e.g.
584 Rudnicki and Rice, 1975; Bésuelle, 2001) in controlling deformation band localisation, and suggests
585 to us that purely strain-based approaches to predicting shear fracture orientations may not be
586 successful.

587

7. Conclusions

1. Cataclastic deformation bands that cut unconsolidated sand (porosity 22-38%) and gravel within the late Pleistocene Mouth of Mad unit exposed in sea cliffs near McKinleyville, Humboldt County, California form two distinct sets that dip shallowly towards the north-northeast and south-southwest. The acute dihedral angle between the two sets of deformation bands is ca. 47° and is bisected by the sub-horizontal, north-northeast incremental and finite shortening (compression) directions.

2. Two-dimensional, area-conserving trishear models of fault propagation folding above the initially buried tip of the McKinleyville Fault predict two sets of LNFE (lines of no finite elongation) that plunge steeply and shallowly to the south and north, respectively. At no point in the models do both the acute dihedral angle between LNFE and the orientation of the acute bisector correspond, respectively, to the acute dihedral angle between the two sets deformation bands and the orientation of the incremental and finite shortening direction. The ellipticities (R) required for the acute dihedral angle between the two sets of LNFE to match the acute dihedral angles observed between conjugate deformation bands is greater than the ellipticities estimated by Fry analysis within the deformation bands and the wall rocks. These results suggest that deformation bands did not form parallel to these LNFE.

3. A Mohr construction for plane strain loading shows that zero extension directions with an acute dihedral angle of 47° develop where the dilatancy rate ($dV/d\varepsilon_1$) is -4.3, equivalent to an angle of dilation (ψ) of 43°. Comparison with previous triaxial deformation experiments on poorly cemented Vosges sandstone suggest that large dilatancy rates (between -8.5 to -2.4) may have been possible during deformation at McKinleyville, provided confining pressure was < 10 MPa and the initial porosity was close to 22%. Conversely, the results of biaxial deformation experiments on unconsolidated Hostun sand suggest that the deformation bands could have developed in a Mohr-Coulomb orientation, assuming a friction angle (φ) of 43° and an initial porosity of 39%. Application of an established empirical relationship between dilatancy rate,

614 mean stress and relative density suggests that dilatancy rates for Vosges sandstone are likely to
615 overestimate the range of dilatancy rates within the Mouth of Mad unit, assuming cohesion was
616 negligible at the time of deformation.

617 4. Previous arguments to explain the occurrence of deformation bands parallel to zero extension
618 directions in coarse grained specimens undergoing biaxial loading are unlikely to apply at
619 McKinleyville where (1) there is no obvious change in the orientation of deformation bands at
620 the interface between sands and inter-bedded gravel lenses; (2) deformation bands have
621 negligible thickness compared with the extent of the Mouth of Mad unit; and (3) deformation
622 bands developed in close proximity to the free surface. We conclude that deformation bands at
623 McKinleyville are most likely to have developed either in an orientation consistent with the
624 Mohr-Coulomb failure criterion, or at an intermediate angle between θ_C and θ_R.

625

626 Acknowledgements

627 We acknowledge BG Group, Shell, Geospatial Research Ltd. and the UK Department of Trade and
628 Industry (now BIS) for funding the ITF-brokered Fractured Reservoirs 3D Digital Atlas Project
629 (FR3DA) at Durham University. Scott Wilkins and Sue Cashman are thanked for introducing RRJ and
630 RHW to the McKinleyville outcrop, and for discussion in the field. Midland Valley Exploration Ltd.
631 provided Move v.2009.1 software to the Department of Earth Sciences at Durham University under
632 their Academic Software Initiative. We acknowledge R.J. Holcombe for free use of GEOrient 9.2 to
633 produce the stereoplots. Richard Lisle, Néstor Cardozo and David Sanderson provided constructive
634 comments; however, any remaining errors or misconceptions are our own.

635

636 References

637 Allmendinger, R.W., 1998. Inverse and forward numerical modeling of trishear fault-propagation
638 folds. Tectonics 17, 640-656.

639 Anderson, E.M., 1951. The dynamics of faulting and dyke formation with applications to Britain.
640 Oliver and Boyd, Edinburgh and London.

641 Arthur, J.R.F., Dunstan, T., Al-Ani, Q.A.J., Assadi, A., 1977. Plastic deformation and failure in
642 granular media. Géotechnique 27, 53-74.

643 Aydin, A., Borja, R.I., Eichhubl, P., 2006. Geological and mathematical framework for failure modes
644 in granular rocks. Journal of Structural Geology 28, 83-98.

645 Bardet, J.P., 1990. A comprehensive review of strain localization in elastoplastic soils. Computers and
646 Geotechnics 10, 163-188.

647 Becker, G.F., 1893. Finite Homogenous Strain, Flow and Rupture of Rocks. Geological Society of
648 America Bulletin 4, 13-90.

649 Berger, G.W., Burke, R.M., Carver, G.A., Easterbrook, D.J., 1991. Test of thermoluminescence
650 dating with coastal sediments from northern California. Chemical Geology 87, 21-37.

651 Bésuelle, P., 2001. Compacting and dilating shear bands in porous rock: Theoretical and experimental
652 conditions. Journal of Geophysical Research 106, 13435-13442.

653 Bésuelle, P., Rudnicki, J.W., 2004. Localization: Shear Bands and Compaction Bands. In: Guéguen,
654 Y., Boutéca, M. (Eds.), Mechanics of Fluid-Saturated Rocks, Elsevier Academic Press, Amsterdam,
655 219-321.

656 Bésuelle, P., Desrues, J., Raynaud, S., 2000. Experimental characterisation of the localisation
657 phenomenon inside a Vosges sandstone in a triaxial cell. International Journal of Rock Mechanics and
658 Mining Sciences 37, 1223-1237.

659 Bolton, M.D., 1986. The strength and dilatancy of sands. Géotechnique 36, 65-78.

660 Bowden, P.B., Jukes, J.A., 1972. The plastic flow of isotropic polymers. Journal of Materials Science
661 7, 52-63.

662 Brace, W.F., 1961. Mohr Construction in the Analysis of Large Geologic Strain. Geological Society
663 of America Bulletin 72, 1059-1080.

664 Cardozo, N., Allmendinger, R.W., Morgan, J.K., 2005. Influence of mechanical stratigraphy and
665 initial stress state on the formation of two fault propagation folds. Journal of Structural Geology 27,
666 1954-1972.

667 Cardozo, N., Jackson, C.A.-L., Whipp, P.S., 2011. Determining the uniqueness of best-fit trishear
668 models. Journal of Structural Geology 33, 1063-1078.

669 Carver, G.A., 1987. Late Cenozoic tectonics of the Eel River basin region, coastal northern California.
670 In: Schymiczek, H., Suchsland, R. (Eds.), Tectonics, Sedimentation and Evolution of the Eel River
671 and other Coastal Basins of Northern California, San Joaquin Geological Society, Miscellaneous
672 Publication 37, 61-71.

673 Carver, G.A., 1992. Late Cenozoic tectonic evolution of coastal northern California. In: Carver, G.A.,
674 Aalto, K.R. (Eds.), Field guide to the Late Cenozoic subduction tectonics & sedimentation of northern
675 coastal California, GB-71, Pacific Section, American Association of Petroleum Geologists, 1-9.

676 Carver, G.A., Aalto, K.R., 1992. Late Cenozoic subduction tectonics and sedimentation, northern
677 coastal California. In: Carver, G.A., Aalto, K.R. (Eds.), Field guide to the Late Cenozoic subduction
678 tectonics & sedimentation of northern coastal California, GB-71, Pacific Section, American
679 Association of Petroleum Geologists, 59-74.

680 Cashman, S., Cashman, K., 2000. Cataclasis and deformation-band formation in unconsolidated
681 marine terrace sand, Humboldt County, California. Geology 28, 111-114.

682 Clarke, S.H., Carver, G.A., 1992. Late Holocene tectonics and paleoseismicity, southern Cascadia
683 Subduction Zone. Science 255, 188-192.

684 Desrues, J., Viggiani, G., 2004. Strain localization in sand: an overview of the experimental results
685 obtained in Grenoble using stereophotogrammetry. International Journal for Numerical and Analytical
686 Methods in Geomechanics 28, 279-321.

687 Desrues, J., Bésuelle, P., Lewis, H., 2007. Strain localization in geomaterials. In: Lewis , H., Couples,
688 G.D. (Eds.), The Relationship between Damage and Localization, Geological Society, London,
689 Special Publications 289, 47– 73.

690 Du Bernard, X., Eichhubl, P., Aydin, A., 2002. Dilation bands: A new form of localized failure in
691 granular media. Geophysical Research Letters 29, no. 24, 2176, doi:10.1029/2002GL015966.

692 Erslev, E.A., 1991. Trishear fault-propagation folding. Geology 19, 617-620.

693 Flavigny, E., Desrues, J., Palayer, B., 1990. Le sable Hostun RF. Revue Française de Géotechnique
694 53, 67-69.

695 Griggs, D.T., 1935. The strain elipsoid as a theory of rupture. American Journal of Science Series 5,
696 30, 121-137.

697 Harvey, E.W., Weppner, E.M., 1992. Pleistocene marginal marine sediments near Mouth of Mad river,
698 Humboldt Country, California. In: Carver, G.A., Aalto, K.R. (Eds.), Field guide to the Late Cenozoic
699 subduction tectonics & sedimentation of northern coastal California, GB-71, Pacific Section,
700 American Association of Petroleum Geologists, 45-50.

701 Heidbach, O., Tingay, M., Barth, A., Reinecker, J., Kurfeß, D., Müller, B., 2008. The World Stress
702 Map database release 2008. doi:10.1594/GFZ.WSM.Rel2008.

703 Houlsby, G.T., Wroth, P.C., 1980. Strain and displacement discontinuities in soil. Journal of the
704 Engineering Mechanics Division, Proceedings of the American Society of Civil Engineers 106, 753-
705 771.

706 Jin, G., Groshong, R.H., 2006. Trishear kinematic modeling of extensional fault-propagation folding.
707 Journal of Structural Geology 28, 170-183.

Jones, R.R., McCaffrey, K.J.W., Imber, J., Wightman, R., Smith, S.A.F., Holdsworth, R.E., Clegg, P., De Paola, N., Healy, D., Wilson, R.W., 2008. Calibration and validation of reservoir models: the importance of high resolution, quantitative outcrop analogues. In: Griffiths, P., Hegre, J., Robinson, A., Price, S. (Eds.), The Future of Geological Modelling in Hydrocarbon Development, The Geological Society, London, Special Publications, 309, 87–98.

Jones, R.R., Kokkalas, S., McCaffrey, K.J.W., 2009. Quantitative analysis and visualization of nonplanar fault surfaces using terrestrial laser scanning (LIDAR) – The Arkitsa fault, central Greece, as a case study. Geosphere 5, 465-482.

Kreemer, C., Holt, W.E., Haines, A.J., 2003. An integrated global model of present-day plate motions and plate boundary deformation, Geophysical Journal International 154, 8-34.

McCrory, P.A., 1996, Evaluation of fault hazards, northern coastal California: U.S. Geological Survey Open-File Report 96-656, 87 p., 2 pls.

McPherson, R.C., 1992. Seismicity and stress at the southern end of the Cascadia subduction zone. In: Carver, G.A., Aalto, K.R. (Eds.), Field guide to the Late Cenozoic subduction tectonics and sedimentation of northern coastal California, GB-71, Pacific Section, American Association of Petroleum Geologists, 21-30.

Miller, W., Morrison, S.D., 1988. Marginal marine Pleistocene fossils from near mouth of Mad River, northern California. Proceedings of the California Academy of Sciences 45, 255-266.

Nguyen, Si.-H., Chemenda, A.I., Ambre, J., 2011. Influence of the loading conditions on the mechanical response of granular materials as constrained from experimental tests on synthetic rock analogue material. International Journal of Rock Mechanics and Mining Sciences 48, 103-115.

Petersen, M.D., Bryant, W.A., Cramer, C.H., Cao, T., Reichle, M., Frankel, A.D., Lienkaemper, J.J., McCrory, P.A., Schwartz, D.P., 1996. Probabalistic seismic hazard assessment for the State of California. California Department of Conservation, Division of Mines and Geology, Open-File Report 96-08.

733 Ramsay, J.G., Huber, M.I., 1983. The techniques of modern structural geology. Volume 1: Strain
734 Analysis. Academic Press, London, 307 pp.

735 Roscoe, K.H., 1970. The influence of strains in soil mechanics. Géotechnique 20, 129-170.

736 Rudnicki, J.W., Rice, J.R., 1975. Conditions for the localization of deformation in pressure-sensitive
737 dilatant materials. Journal of the Mechanics and Physics of Solids 23, 371-394.

738 Sarkarinejad, K., Samani, B., Faghih, A., 2011. A Mohr circle method for 3D strain measurement
739 using the geometry of no finite longitudinal strain and the R_{xz} ratio. Journal of Structural Geology 33,
740 424-432.

741 Schanz, T., Vermeer, P.A., 1996. Angles of friction and dilatancy of sand. Géotechnique 46, 145-151.

742 United States Geological Survey, 2011. Geologic Science Hazards Center, California Quaternary
743 Faults, http://geohazards.usgs.gov/qfaults/ca/California.php, accessed 19th August 2011. Hart, E.W.,
744 compiler, 1999, Fault number 13, Mad River fault zone, in Quaternary fault and fold database of the
745 United States: U.S. Geological Survey website, http://earthquakes.usgs.gov/regional/qfaults, accessed
746 07/03/2012 09:54 AM.

747 Vermeer, P.A., 1990. The orientation of shear bands in biaxial tests. Géotechnique 40, 223-236.

748 Vermeer, P.A., de Borst, R., 1984. Non-associated plasticity for soils, concrete and rock. HERON 29,
749 3-64.

750 Wang, Y.H., Leung, S.C., 2008. Characterization of Cemented Sand by Experimental and Numerical
751 Investigations. Journal of Geotechnical and Geoenvironmental Engineering 134, 992-1004.

752 Watterson, J., 1999. The future of failure: stress or strain? Journal of Structural Geology 21, 939-948.

753 Withjack, M.O., Olson, J., Peterson, E., 1990. Experimental models of extensional forced folds.
754 AAPG Bulletin 74, 1038-1054.

Wolf, H., König, D., Triantafyllidis, T., 2003. Experimental investigation of shear band patterns in granular material. Journal of Structural Geology 25, 1229-1240.

Figure captions

Fig. 1. (a) Graph showing the acute angle between LNFE (2α) *versus* ellipticity, (Rxz) for a constant area deformation. Inset shows the finite strain ellipse, an undeformed circular marker and the two lines of no finite elongation (LNFE). 2α is the acute angle between the two sets of LNFE; α is the angle between the LNFE and the maximum principal axis of finite strain. λ_1 and λ_2 are the maximum and minimum quadratic extensions. X and Z are the maximum and minimum principal axes of finite strain. (b) Mohr's circle for strain increment. $d\varepsilon$ and $d\gamma$ are the axes of incremental longitudinal and shear strain, respectively. $d\varepsilon_1$ and $d\varepsilon_3$ are the principal axes of shortening and extension increment, respectively. θ_R is the angle between $d\varepsilon_1$ and the zero extension directions. ψ is the angle of dilation. Inset shows two sets of deformation bands (bold lines) that are assumed to have developed along zero extension directions. Modified from Bardet (1990, fig. 1).

Fig. 2. (a) Simplified tectonic map showing the main structures associated with the southern part of the Cascadia Subduction Zone in northern California. MRfz = Mad River fault zone; LSfz = Little Salmon fault zone; Fs = Freshwater syncline; Mtj = Medocino triple junction. SG-NA gives the motion of the South Gorda plate relative to a fixed North American Plate. Box shows approximate location of Fig. 2b. (b) Map showing the coastline of part of Humboldt County (solid line) and strain rate (arrows) and maximum horizontal stress (S_{Hmax}) directions. Length of arrows is proportional to the strain rate. Star (*) gives approximate location of the study area. Strain rates from Kreemer et al. (2003); stresses from Heidbach et al. (2008). Map based on image created using the UNAVCO Jules Verne Voyager. (c) NE-SW cross-section through the Mad River fault zone showing Cretaceous basement rocks (diagonal shading) thrust over early Pleistocene Falor Formation sediments (grey). Location shown in Fig. 2b. (a) and (c) are simplified from Carver (1992).

Fig. 3. (a) Structural map showing the thrust faults in the McKinleyville area and the location of the studied section. Simplified from the USGS California Quaternary Faults database (USGS, 2011). Box gives the approximate location of Fig. 3b. (b) Overview from Google Earth showing part of the McKinleyville fault and the studied section. Line of section (white double-headed arrow) is ca. 150 m

783 long. (“101”) is Highway 101; (1) and (2) are the traces of the southern and northern segments of the
784 McKinleyville fault, respectively.

785 Fig. 4. (a) Photograph showing part of the studied outcrop (at approximately 40º58’17’’N;
786 124º07’07’’W). North is to the left; reflective cylinder (circled) is 11 cm in diameter. Two prominent
787 sets of cataclastic deformation bands cut the unconsolidated sands. The acute angle between the two
788 sets of deformation bands is highlighted and the sub-horizontal acute bisector is represented by an
789 arrow. (b) Photograph showing a gravel bed that has been cut and offset by a south-dipping cataclastic
790 deformation band (arrow). There is no discernible change in the orientation of this deformation band
791 as it passes from sand into gravel. North is to the left; survey peg (circled) is 10 cm high. (c) Lower
792 hemisphere equal area stereoplot showing poles to cataclastic deformation bands, n = 2256. Great
793 circles show the mean deformation band orientations estimated from a contoured stereoplot; asterisk
794 is the acute bisector of the great circles. (d) Contoured stereoplot for the dataset in (c). Contours are %
795 per 1% area, with contour interval as shown. Great circles and asterisk the same as in (c).

796 Fig. 5. (a) – (o) Lower hemisphere equal area stereoplots showing poles to cataclastic deformation
797 bands for 5 m intervals along the outcrop, as listed in Table 1. Great circles are the best-fit planes to
798 each cluster, estimated from contoured stereoplots. (a) is at the northern extremity of the outcrop; (o)
799 is at the southern limit. (p) Lower hemisphere equal area stereoplot showing the acute bisectors of the
800 pairs of great circles shown in (a) – (o). n is the number of data points in each stereoplot. (q)
801 Overview from Google Earth showing the studied outcrop. (a-c), (d-h) and (i-o) show the approximate
802 locations of each stereoplot. (1) and (2) are the traces of the southern and northern segments of the
803 McKinleyville fault, respectively. (“101”) is Highway 101.

804 Fig. 6. Schematic diagram showing the template used for the two-dimensional trishear modelling. The
805 vertical section is oriented 010°-190°. The circles represent unit circles inscribed on four layers within
806 the template and used to determine the ellipticities and LNFE orientations after deformation.
807 Locations of unit circles are schematic to enhance clarity – unit circles were spaced every 5 m in the
808 models. The approximate location of the landslip shown in Figs 3b and 5q is highlighted.

809 Fig. 7. Graphs showing the variation in ellipticity (Rxz) calculated by the trishear forward model
810 across the studied section for total thrust offsets along the southern segment of the McKinleyville fault
811 of (a) 10 m and (b) 56 m. Both graphs show models with trishear apical angles of 50° and 90°. Note
812 the different vertical scales in (a) and (b). In (a) the thrust has not yet propagated through the marker
813 layer (Fig. 6); in (b) the thrust has propagated through the marker layer. The grey shading illustrates
814 the approximate location of the landslip shown in Figs 3b and 5q. The dashed line shows the location
815 of the present day outcrop in each model. Note that in the model, the footwall is pinned so the hanging
816 wall (including the landslip) effectively moves to the right (south) with increasing thrust displacement.

817 Fig. 8. Graphs showing the plunge of the two sets of LNFE, acute dihedral angle between LNFE and
818 plunge of the acute bisector between LNFE *versus* distance along the studied section. (a) Model with
819 a maximum thrust offset of 10 m and apical angle of 50°. (b) Model with a maximum thrust offset of
820 10 m and apical angle of 90°. (c) Model with a maximum thrust offset of 56 m and apical angle of 50°.
821 (d) Model with a maximum thrust offset of 56 m and apical angle of 50°. For clarity in (c) and (d),
822 data have been plotted separately for the footwall and hanging wall of the faults. In all parts, the grey
823 shading illustrates the approximate location of the landslip shown in Figs 3b and 5q. Positive angles
824 refer to southward plunging LNFE and southward plunging acute bisectors; negative angles refer to
825 northward dips and plunges.

826 Fig. 9. Graph of ellipticity (Rxz) *versus* distance along the section assuming *a priori* the two sets of
827 deformation bands developed parallel to LNFE. Ellipticities have been calculated from the mean
828 dihedral angles between the two sets of deformation bands (Table 1) using the relationship between
829 ellipticity and dihedral angle (2α) shown in Fig. 1a. North is to the left. The shaded bar shows the
830 range of ellipticities obtained by Cashman and Cashman (2000) from Fry analysis of cataclastic
831 deformation band samples.

832 Fig. 10. (a) Mohr constructions for plane strain deformation ($d\varepsilon_2 = 0$). $d\varepsilon$ and $d\gamma$ are the axes of
833 incremental longitudinal and shear strain, respectively. $d\varepsilon_1$ and $d\varepsilon_3$ are the principal axes of
834 incremental shortening and extension, respectively. Dashed lines are used to determine the zero

835 extension directions. $2\theta_R$ is the acute angle between pairs of zero extension directions (Fig. 1b). Grey
836 Mohr's circle is for isovolumetric deformation. Black Mohr's circle shows the dilation required for
837 $2\theta_R = 47°$ during plane strain deformation. (b) Graph showing the variation in dilatancy rate (plotted
838 as $-dv/d\varepsilon_1$) *versus* distance along the studied section assuming *a priori* that the two sets of cataclastic
839 deformation bands formed along zero extension directions. Dilatancy rates have been calculated from
840 the mean dihedral angles between the two sets of deformation bands (Table 1) using a Mohr
841 construction similar to (a).

842 Fig. 11. (a) Graph showing dilatancy rate (plotted as $-dv/d\varepsilon_1$) *versus* confining pressure for Vosges
843 sandstone and Hostun sand. Dilatancy rates estimated from data presented by Bésuelle et al. (2000, fig.
844 3) (Vosges sandstone) and Desrues and Viggiani (2004, figs 11 and 13 and Table IV) (Hostun sand).
845 (b) Graph showing the orientations of deformation bands produced during triaxial deformation of
846 Vosges sandstone *versus* confining pressure. "Roscoe orientation" shows the orientation of zero
847 extension directions determined from the dilatancy rates in (a) assuming oblate strain ($d\varepsilon_2 = d\varepsilon_3$).
848 "Coulomb orientation" shows the orientation of deformation bands predicted by the Mohr-Coulomb
849 failure criterion (equation 1). Friction angles have been estimated from the failure envelope presented
850 by Bésuelle et al. (2000, fig. 20). (c) Graph showing the orientations of deformation bands produced
851 during biaxial deformation of Hostun sand *versus* confining pressure. "Roscoe orientation" shows the
852 orientation of zero extension directions determined from the dilatancy rates in (a) assuming plane
853 strain ($d\varepsilon_2 = 0$). Friction angles have been obtained from Desrues and Viggiani (2004, their Table IV).

854

Distance from start of section (m)	*****	**n**	**Set 1 (dip/dip direction)**	**Set 2 (dip/dip direction)**	**Dihedral angle**	**Bisector orientation (plunge/azimuth)**
15 (north)	a	165	58/307	21/190	69	21/325
20	b	124	26/044	22/187	45	02/027
30	c	113	29/032	24/195	52	03/024

85	d	82	18/026	35/225	52	09/218
90	e	272	20/021	32/216	52	06/210
95	f	196	21/021	35/226	55	07/216
100	g	212	22/022	30/234	50	02/220
105	h	146	18/051	25/202	42	04/214
120	i	60	11/005	20/184	31	05/184
125	j	134	19/025	25/198	44	03/201
130	k	204	19/037	23/192	41	02/203
135	l	142	22/043	22/207	44	00/215
140	m	55	18/031	32/190	49	07/198
145	n	84	17/036	27/198	43	05/205
150 (south)	o	95	21/046	24/223	45	02/224

855

856 Table 1. Summary of the mean cataclastic deformation band orientations, acute dihedral angles and
857 bisector orientations from north to south across the studied outcrop; n = number of deformation bands
858 measured within each 5 m interval. * each letter corresponds to the appropriate stereoplot in Figure 4.

859

860

861

862

863

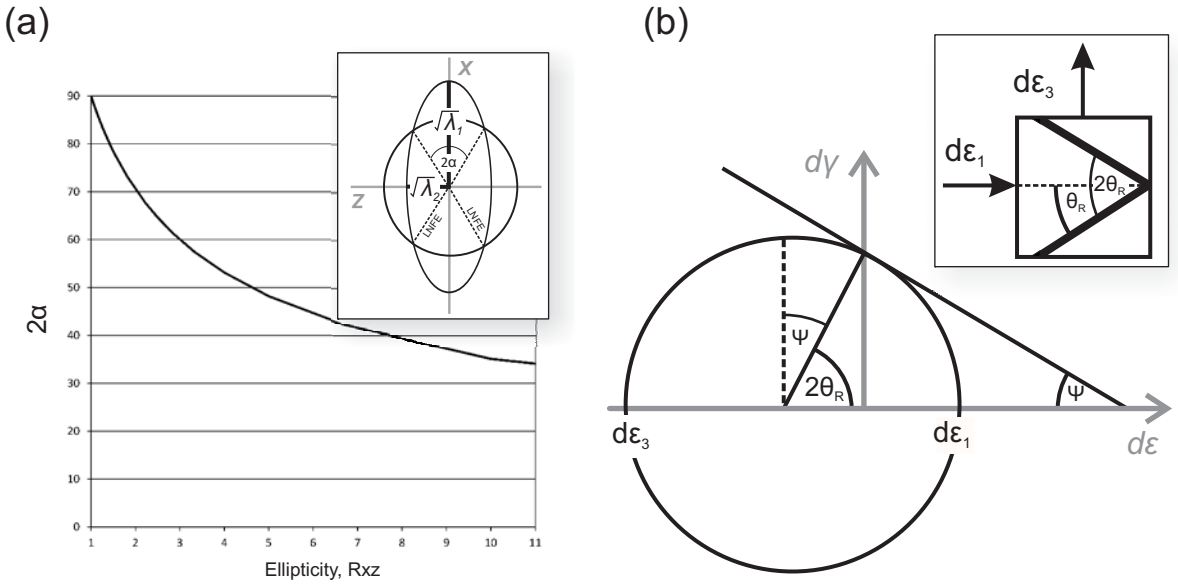

Imber et al. Fig. 1

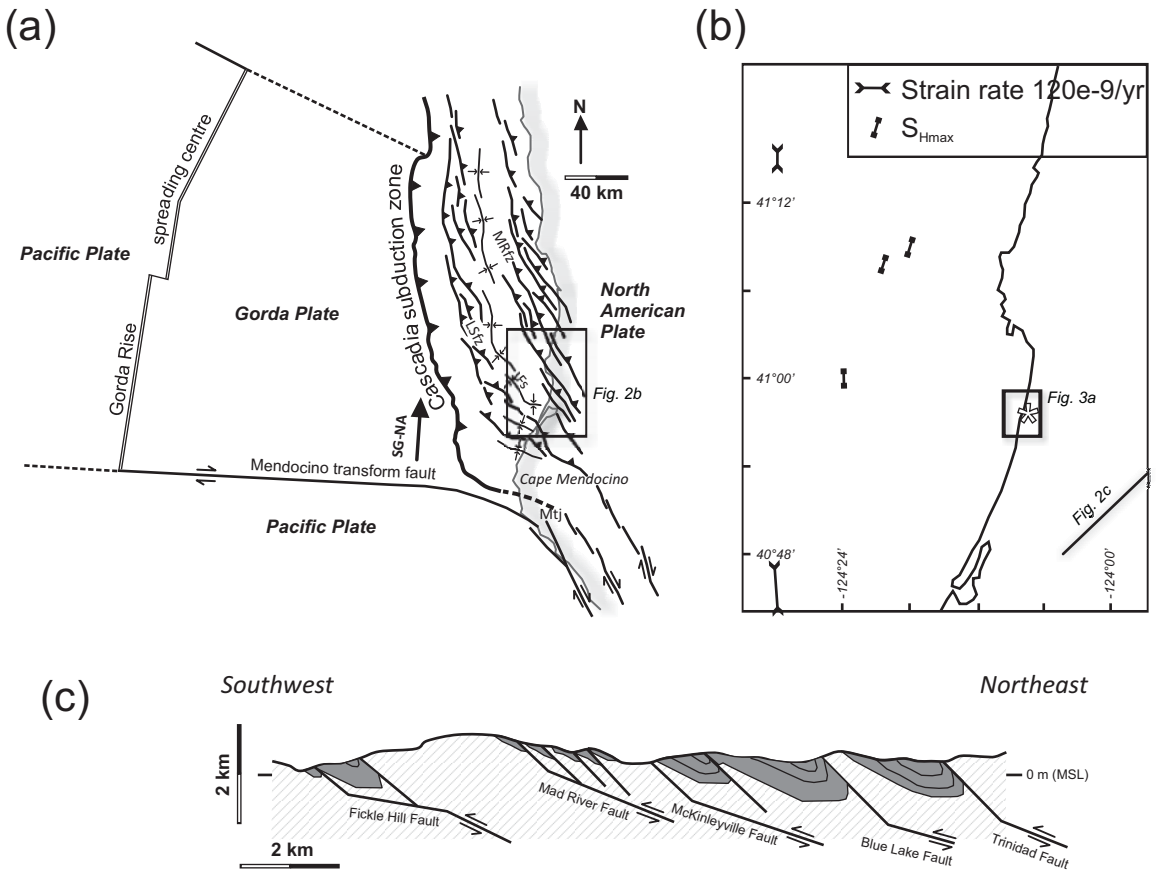

Imber et al. Fig. 2

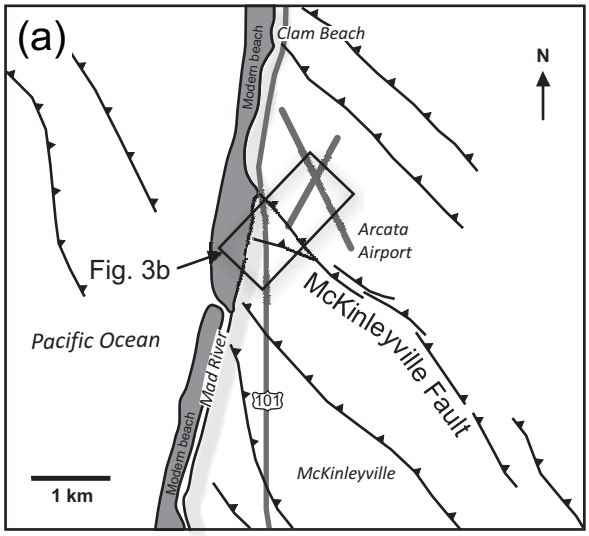

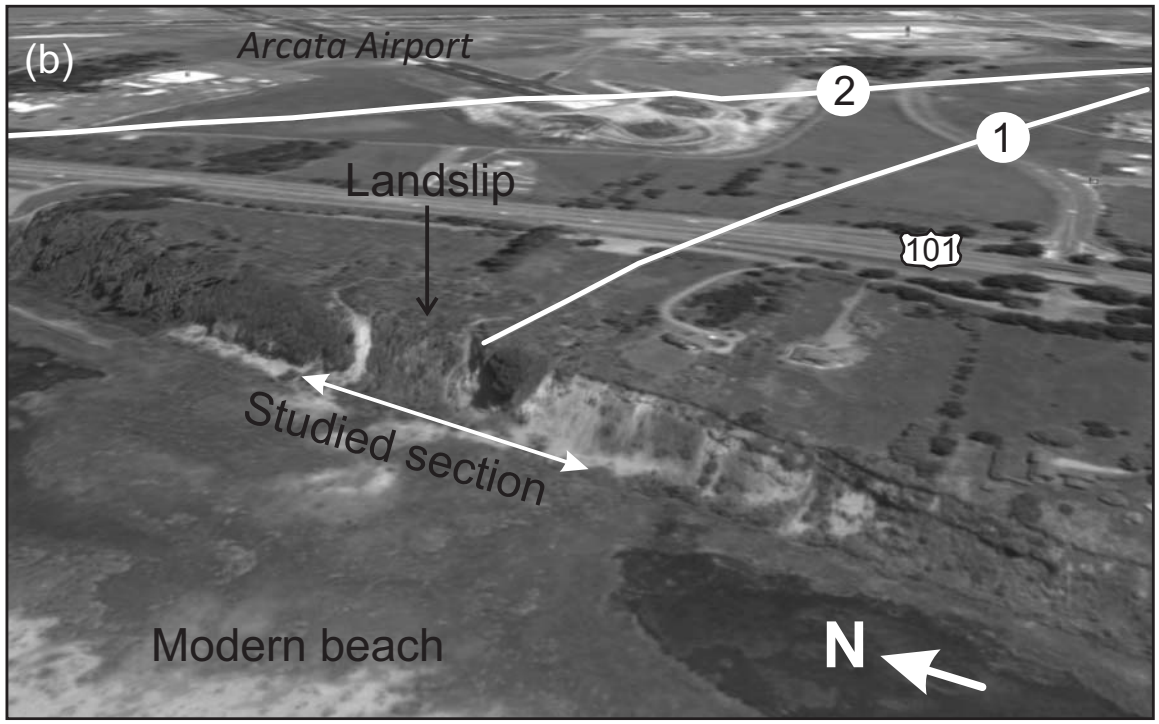

Imber et al. Fig. 3

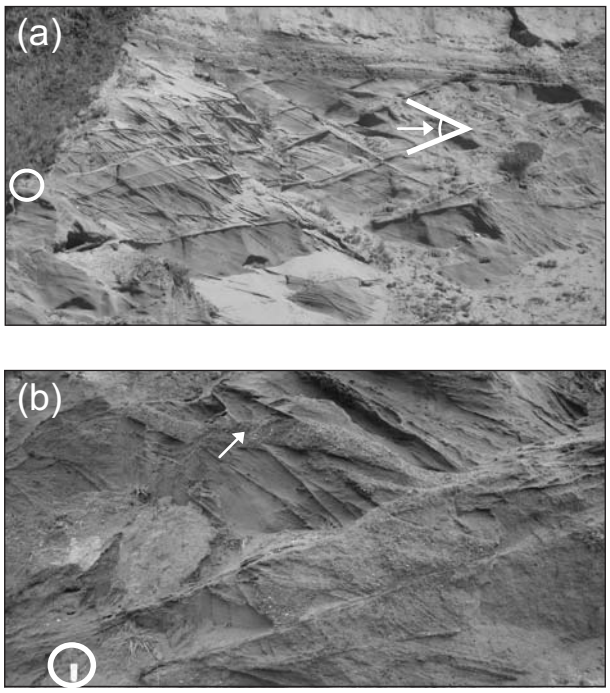

Imber et al. Fig. 4

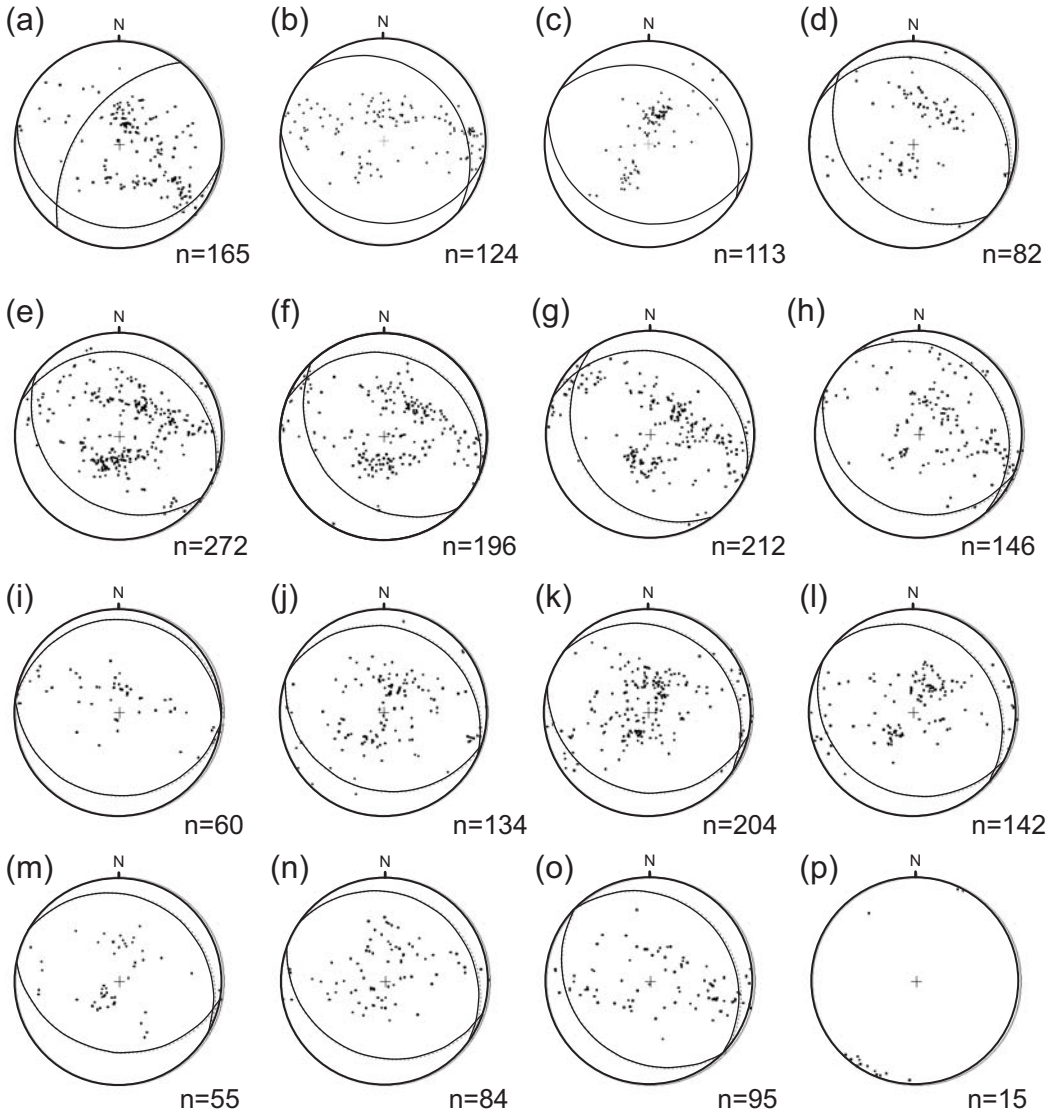

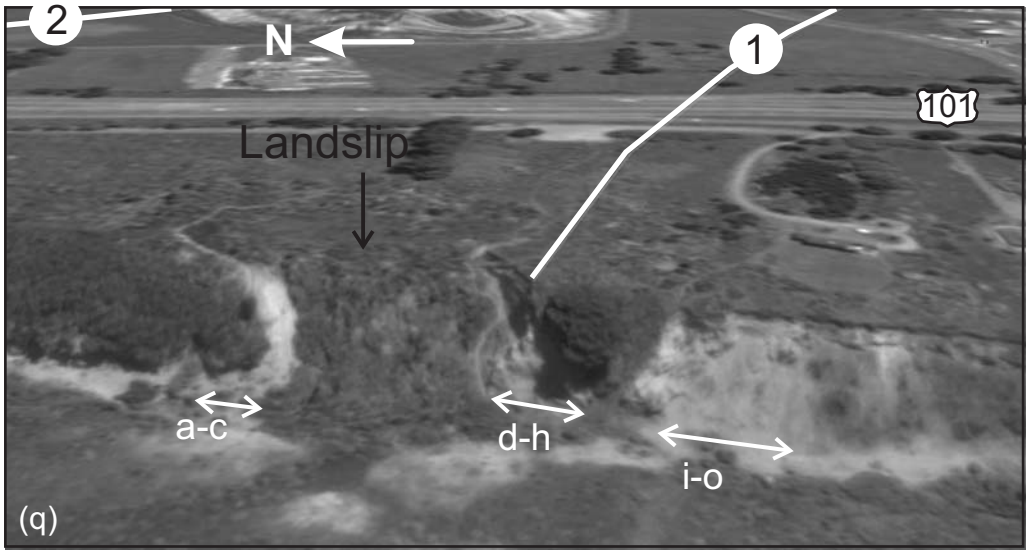

Imber et al. Fig. 5

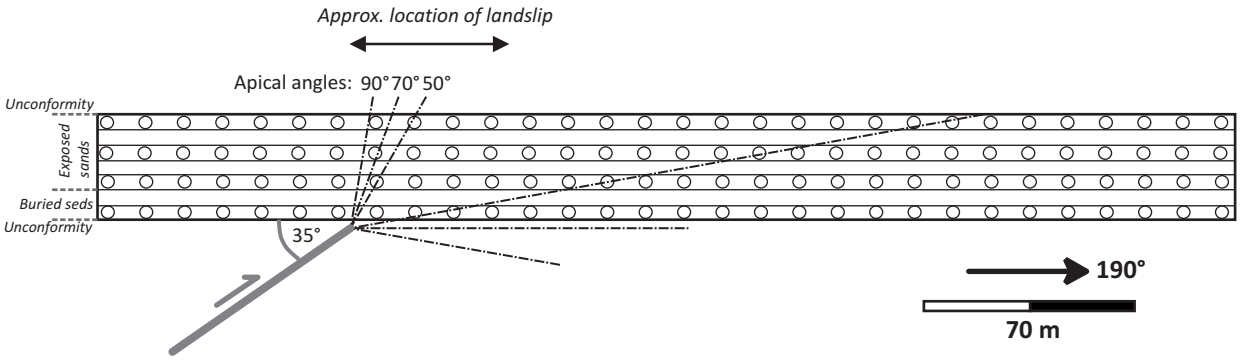

Imber et al. Fig. 6

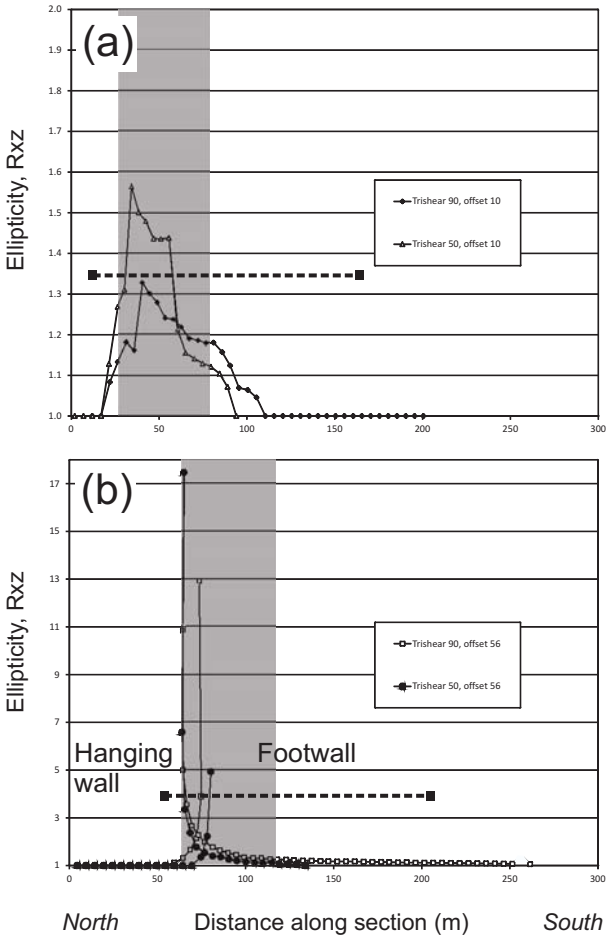

Imber et al. Fig. 7

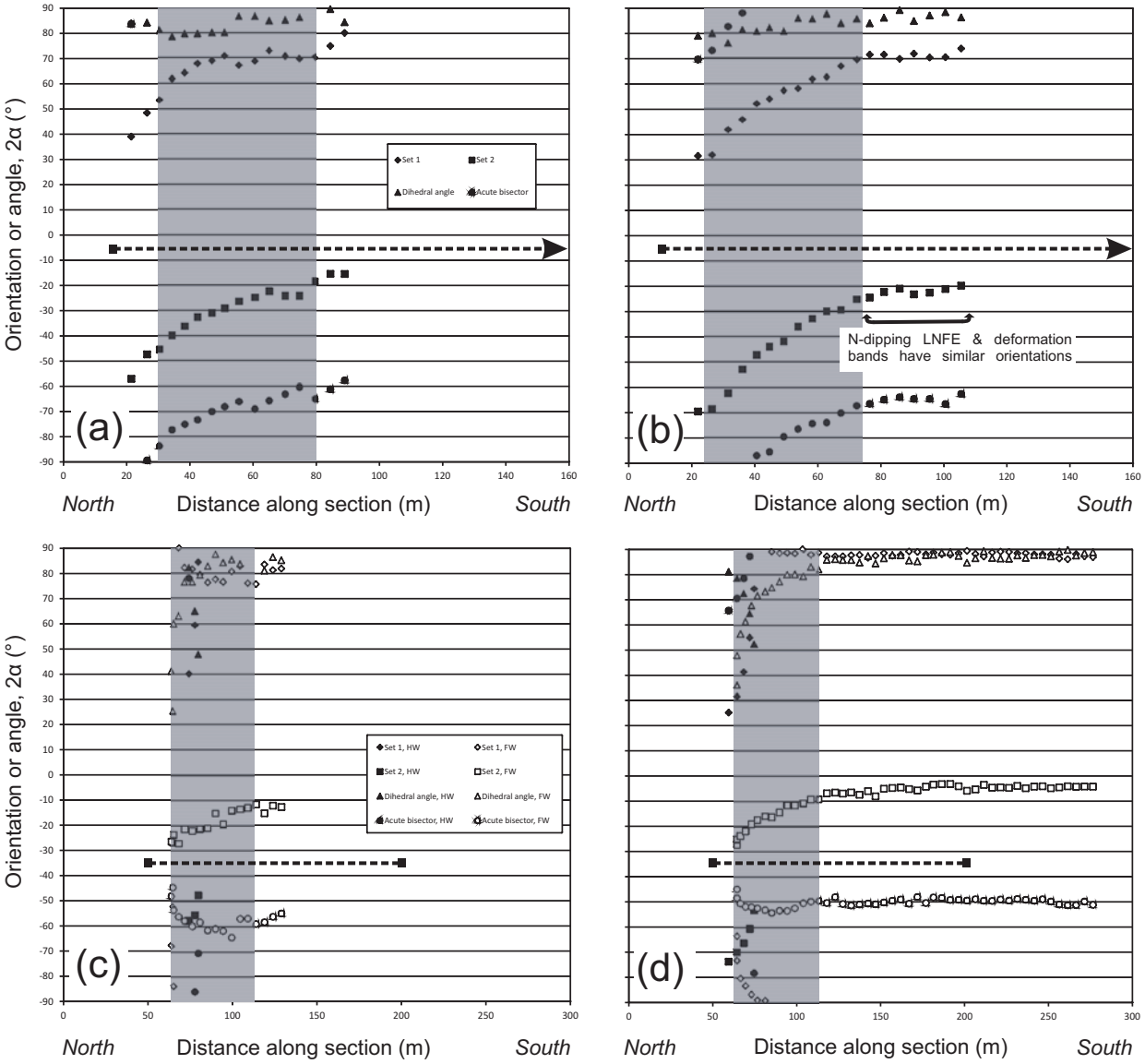

Imber et al. Fig. 8

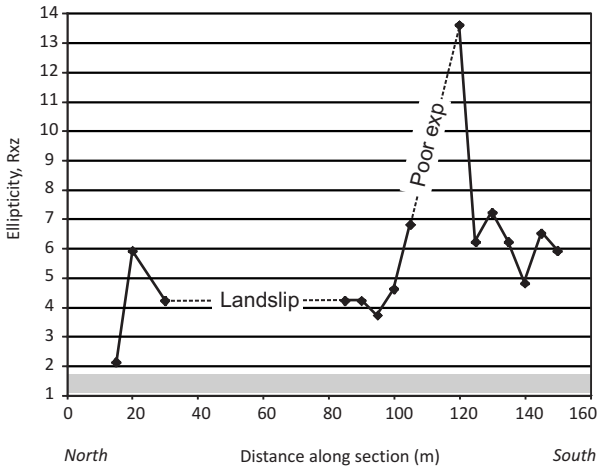

Imber et al. Fig. 9

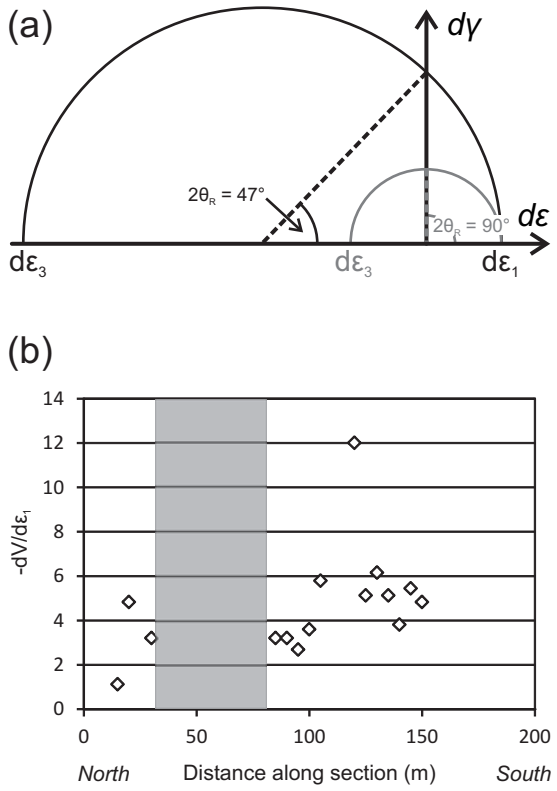

Imber et al. Fig. 10

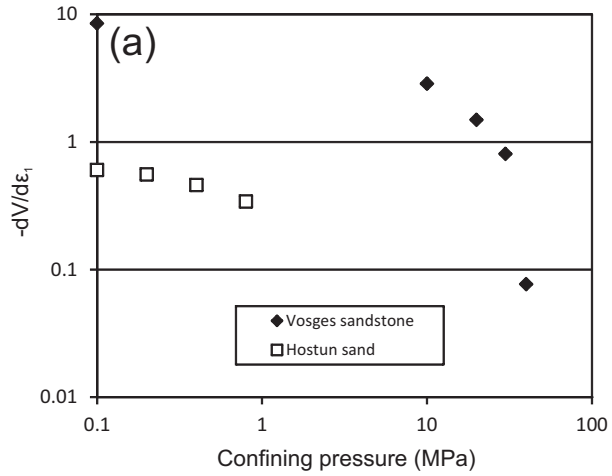

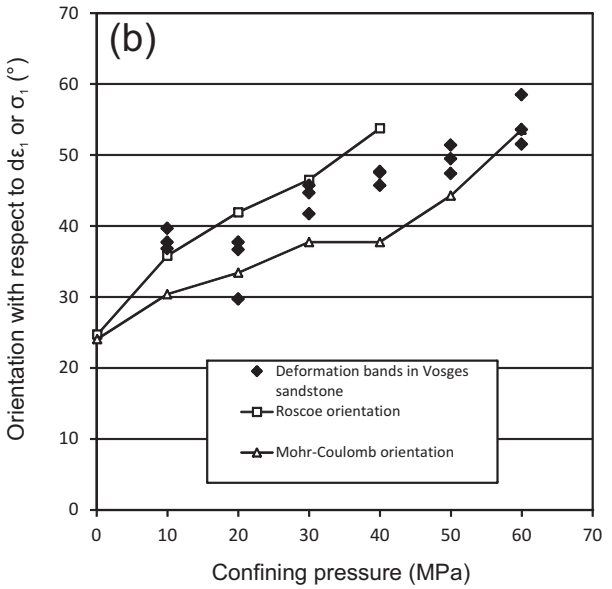

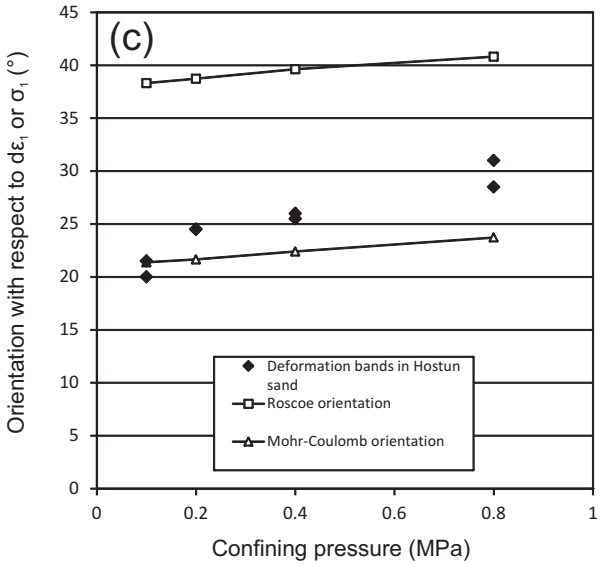

Imber et al. Fig. 11